JGR Earth Surface

RESEARCH ARTICLE
10.1029/2021JF006384

Improved Estimation of Glacial-Earthquake Size Through New Modeling of the Seismic Source

Kira G. Olsen[1], Meredith Nettles[1], L. Mac Cathles[2], Justin C. Burton[3], Tavi Murray[4], and Timothy D. James[5]

[1]Lamont-Doherty Earth Observatory, Columbia University, New York, NY, USA, [2]Climate and Space Sciences and Engineering, University of Michigan, Ann Arbor, MI, USA, [3]Department of Physics, Emory University, Atlanta, GA, USA, [4]Glaciology Group, Department of Geography, College of Science, Swansea University, Swansea, UK, [5]Department of Geography and Planning, Queen's University, Kingston, ON, Canada

Key Points:

- A physics-based source model for glacial-earthquake modeling improves recovery of seismic-magnitude values
- Maximum force is less sensitive to model choices than M_{CSF} and is preferred for describing glacial-earthquake size
- A rapid force reversal during iceberg calving is the most important feature to capture in a glacial-earthquake source model

Correspondence to:

M. Nettles,
nettles@ldeo.columbia.edu

Citation:

Olsen, K. G., Nettles, M., Cathles, L. M., Burton, J. C., Murray, T., & James, T. D. (2021). Improved estimation of glacial-earthquake size through new modeling of the seismic source. *Journal of Geophysical Research: Earth Surface*, *126*, e2021JF006384. https://doi.org/10.1029/2021JF006384

Received 3 AUG 2021
Accepted 23 NOV 2021

Abstract The number of gigaton-sized iceberg-calving events occurring annually at Greenland glaciers is increasing, part of a larger trend of accelerating mass loss from the Greenland Ice Sheet. Though visual observation of large calving events is rare, ~60 glacial earthquakes generated by these calving events are currently recorded each year by regional and global seismic stations. An empirical relationship between iceberg size and M_{CSF}, a summary measure of glacial-earthquake size, was recently demonstrated by Olsen and Nettles (2019), https://doi.org/10.1029/2019JF005054. However, M_{CSF} is known to be sensitive to choices made in modeling the seismic source. We incorporate constraints on the seismic source from laboratory studies of calving and test multiple source time functions using synthetic and observed glacial-earthquake waveforms. We find that a simple, fixed time function with a shape informed by laboratory results greatly improves estimates of earthquake size. The average ratio of estimated to true peak force values is 1.03 for experiments using our preferred source model, compared with an average of 0.3 for models used in previous studies. We find that maximum-force values estimated from waveform modeling depend far less on model choices than does M_{CSF}, and therefore prefer maximum force as a measure of glacial-earthquake size. Using both synthetic and real data, we confirm a correlation between maximum force and iceberg mass. Our results support the possibility of developing useful scaling relationships between seismic observables and physical parameters controlling glacier calving.

Plain Language Summary The Greenland Ice Sheet is losing ice mass. About half of that ice is lost when large icebergs break off, or calve, from the fronts of glaciers into the ocean. Knowing the sizes of these icebergs would be valuable, but iceberg calving is rarely captured on camera. However, the largest icebergs produce seismic signals when they calve, referred to as glacial earthquakes. We investigate the relationship between the size of an iceberg and the magnitude of the glacial earthquake it produces, building new models to describe the forces that generate a glacial earthquake. Previously, most details of the force evolution during iceberg calving were unknown. We use observations from laboratory experiments conducted using a plastic block in a tank of water, built to mimic the glacier-ocean setting. We find that incorporating information from these laboratory experiments into our seismic model greatly improves estimates of earthquake size. Using our new models, we confirm a correlation between glacial-earthquake magnitude and iceberg size, and show that our improved estimates are likely to be more realistic. Our results suggest that using seismic information to estimate iceberg size and related quantities is a promising path forward.

1. Introduction

Ice loss from the Greenland Ice Sheet has accelerated in recent years, and up to half of that mass loss results from iceberg calving (Enderlin et al., 2014). More than 200 large glaciers around Greenland advect ice from the interior of the ice sheet to the ocean (Moon et al., 2012), and during the summer months, multiple large iceberg-calving events can occur at a single glacier over the course of a day (e.g., Olsen & Nettles, 2019). Some of the largest calving events involve icebergs of ~1 km^3 that are driven to capsize against the glacier terminus by buoyancy forces. These rotational calving events generate glacial earthquakes (Ekström et al., 2003), magnitude ~5 seismic events that can be detected using the broadband stations of the Global Seismographic Network and the Greenland Ice Sheet Monitoring Network (GLISN). During calving, the motion of the iceberg and the water it displaces exert a

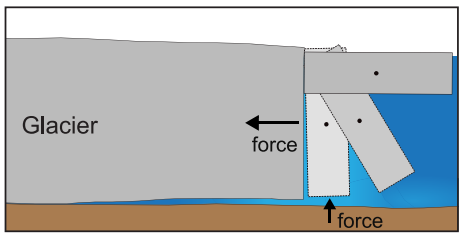

Figure 1. Geometry of iceberg capsize from vertical (lightest gray iceberg) to horizontal (darkest gray iceberg). Black dot indicates iceberg's center of mass. In the simple model used in Figure 2, the distance the iceberg travels during capsize is taken to be the horizontal difference between the center-of-mass location at the start and end of capsize. Figure modified from Murray, Nettles, et al. (2015). Reprinted with permission from AAAS.

time-varying force on the Earth. The seismic waves generated by these forces contain information about the physics of the calving process, and about the iceberg that calved.

Glacial earthquakes are generated by a style of mass loss known as buoyancy-driven calving, which, at tidewater glaciers, occurs when a glacier terminates close to its grounding line. If the glacier terminus is driven below isostatic equilibrium as it flows into the water, buoyancy forces will push upward on the short floating ice tongue, driving basal crevassing and subsequent iceberg calving (James et al., 2014; Murray, Selmes, et al., 2015). Icebergs lost through buoyancy-driven calving may extend the full glacier thickness (up to ∼1 km) and have been observed to have aspect ratios of ∼0.1–0.5, where the short dimension is measured along flow (Amundson et al., 2010; James et al., 2014; Murray, Nettles, et al., 2015; Olsen & Nettles, 2019; Walter et al., 2012). This tall, narrow geometry is unstable and leads the iceberg to capsize against the terminus (Figure 1). The majority of these calving events involve bottom-out iceberg rotation, where the top of the iceberg remains pinned against the terminus during the first stages of rotation while the lower portion of the iceberg rotates up in the water column and away from the terminus. A limited number of top-out calving events have also been observed (e.g., Walter et al., 2012), but this calving geometry is rare.

During iceberg capsize, time-varying horizontal and vertical forces are applied to the Earth and generate the seismic waves recorded as a glacial earthquake. The largest-amplitude force, horizontal and oriented perpendicular to the calving face, is generated by the iceberg accelerating into the fjord and away from the glacier terminus during capsize (Figure 1; Nettles & Ekström, 2010; Murray, Nettles, et al., 2015). A small vertical force is simultaneously generated behind the rotating iceberg by a pressure drop in the water column (Murray, Nettles, et al., 2015). The sum of these forces is a subhorizontal force acting at the glacier terminus. The orientation and magnitude of the force, along with estimates of event location and timing, can be obtained by analysis of the seismic waves produced.

Systematic analysis of glacial-earthquake seismic data (Olsen & Nettles, 2017; Tsai & Ekström, 2007; Veitch & Nettles, 2012) has led to a catalog of glacial earthquakes that now spans more than two decades and forms a robust seismic record of iceberg calving including nearly 450 glacial earthquakes. The rate of earthquake occurrence has increased with time (e.g., Ekström et al., 2006; Olsen & Nettles, 2017); currently, ∼60 glacial earthquakes occur in Greenland each year. Study of glacial earthquakes has advanced our understanding of numerous aspects of mass loss around Greenland, including the spatial evolution of buoyancy-driven calving (Nettles & Ekström, 2010; Olsen & Nettles, 2017; Veitch & Nettles, 2012), seasonal patterns in calving (Ekström et al., 2006; Olsen & Nettles, 2017; Veitch & Nettles, 2012), and evolution of terminus dynamics at individual glaciers (Murray, Selmes, et al., 2015; Olsen & Nettles, 2017, 2019; Veitch & Nettles, 2012; Walter et al., 2012).

An ongoing goal of glacial-earthquake analysis has been to relate the seismic magnitude of a glacial earthquake to the size of a calving iceberg. Clarifying such a relationship would allow permanent seismic stations to be used for remote quantification of mass loss through calving at numerous glaciers in Greenland in near-real time. In a recent study (Olsen & Nettles, 2019), we used iceberg-size estimates from 12 calving events to publish the first empirical demonstration of a correlation between iceberg size and a measure of glacial-earthquake magnitude, M_{CSF}, obtained using centroid-single-force (CSF) analysis of the seismic waveforms. We have subsequently analyzed nine additional calving events, and find results in close agreement with the previously reported trend (Figure 2). The relationship between M_{CSF} and iceberg size that we observe follows the trend predicted by a very simple geometric model relating the seismic magnitude of a gravitationally driven seismic event to the mass of the accelerating object multiplied by the distance over which it accelerates (Kawakatsu, 1989). For a glacial earthquake, the minimum value for M_{CSF} corresponds to the iceberg mass multiplied by the distance required for the iceberg to capsize (see Figure 1). However, the seismically determined M_{CSF} values are approximately an order of magnitude smaller than predicted by this simple, geometric model, given the observed dimensions of each iceberg (Figure 2). The empirical demonstration of a clear relationship between seismic magnitude and iceberg size, combined with the observed relationship with the simple model, suggests that a more detailed investigation is merited.

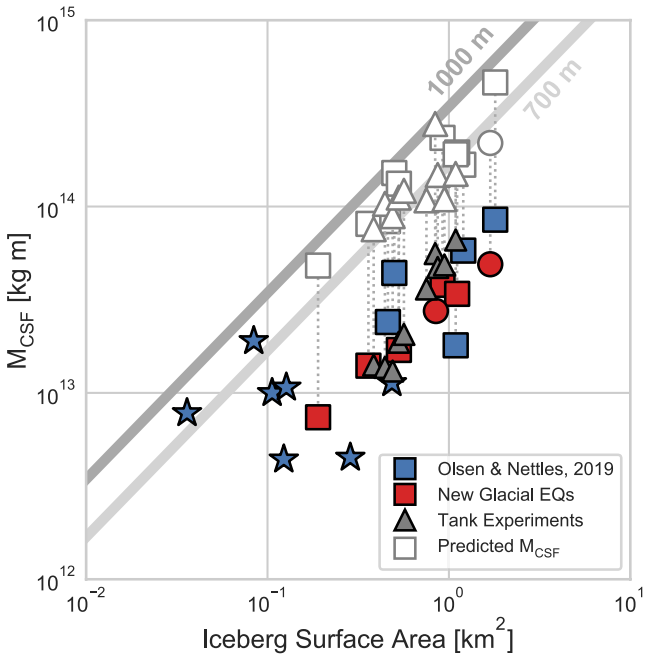

Figure 2. Comparison between iceberg surface area and M_{CSF} modeled using a standard 50-s boxcar time function, illustrating the systematic mismatch between calculated M_{CSF} values and those expected from the simple model described in the text. Blue symbols (both squares and stars) represent glacial earthquakes occurring at Jakobshavn Isbræ and Helheim Glacier, from Olsen and Nettles (2019). Red symbols represent glacial earthquakes ("EQs") occurring at Helheim Glacier and analyzed for this study. These calving events were reported by Murray, Selmes, et al. (2015), and iceberg area estimates shown here were obtained following that study and Murray, Nettles, et al. (2015). Gray triangles represent tank experiments (Figure 5). Squares represent single glacial earthquakes. Each red circle represents a pair of glacial earthquakes that occurred on the same day and for which M_{CSF} and iceberg-area values are summed for the two events. Stars represent very small glacial earthquakes (Figure 9 of Olsen & Nettles, 2019). White symbols represent predicted M_{CSF} values for the glacial earthquakes and tank experiments (as indicated by the joining dashed lines), according to the simple model and given the observed iceberg dimensions. Model predictions are not provided for very small glacial earthquakes (blue stars) due to less reliable M_{CSF} estimates and limited knowledge of iceberg height. Gray solid lines show values predicted from the simple model for an iceberg aspect ratio of 0.25 and iceberg height fixed at either (dark gray) 1,000 m or (light gray) 700 m, as described in Section 5.5 of Olsen and Nettles (2019).

The assumption most likely to affect seismically derived estimates of M_{CSF} is that of the time history of the applied force, or force-time function, specified in waveform modeling. M_{CSF} values have long been known to be sensitive to the duration of the force-time function (i.e., the seismic source model) used in analysis. Tsai et al. (2008) considered a range of force-time functions and found that glacial-earthquake waveforms could be modeled well using a 50-s, symmetric, double-boxcar force model, or asymmetric boxcar models of varying durations. Veitch and Nettles (2012) demonstrated that retaining the boxcar shape but varying the duration of the force function by 20% changed the estimated M_{CSF} value by 20%–30%. Extending this analysis, we find that doubling the source-model duration can increase the estimated M_{CSF} value by a factor of four or more, though estimates of force geometry change very little. Because the true duration and character of the seismic source is not known for individual calving events, all glacial earthquakes in the published catalog (Olsen & Nettles, 2017, 2019; Tsai & Ekström, 2007; Veitch & Nettles, 2012) have been analyzed using the same, fixed model as an approximation of the seismic source.

Ideally, the seismic analysis could be made insensitive to the duration and shape of the force-time history; or, a description of the force-time history could be extracted directly from the waveforms. However, glacial-earthquake signals are dominated by energy within a narrow frequency band, restricting such approaches. Centroid-single-force (CSF) analysis of glacial earthquakes (e.g., Ekström et al., 2003) is typically conducted using surface waves recorded in the period band 50–150 s, the same period band used in centroid-moment-tensor (CMT) analysis of tectonic earthquakes of similar size (e.g., Ekström et al., 2012). In this band, signal strength is high, Earth noise is relatively low, and the Earth's lateral velocity heterogeneity is well described. Because tectonic earthquakes of this size have durations of only a few seconds, much shorter than the period of the waves analyzed, estimates of earthquake size are only weakly sensitive to the choice of source time function. In contrast, the long durations of glacial earthquakes (at least several 10s of seconds) are similar to the period of the waves analyzed, making estimates of earthquake size more strongly sensitive to the choice of source time function. At periods longer than the glacial-earthquake duration, seismic-wave amplitudes are very small, owing to the small sizes of even the largest glacial earthquakes (M~5), such that, even at quiet, nearby seismic stations, glacial-earthquake energy is below noise levels at periods longer than 100–150 s. Further, while the robust high-frequency energy generated by most tectonic earthquakes can allow reconstruction of the source time function directly from recorded seismic waves, the slow source of glacial earthquakes (iceberg rotation over 10–100s of seconds) results in seismic waves that are severely depleted in high-frequency energy at periods shorter than ~30–50 s. This high-frequency depletion for glacial-earthquake events has long been recognized (Ekström et al., 2003), and is the reason glacial earthquakes go undetected by short-period body-wave detection algorithms; Olsen and Nettles (2019) recently confirmed that glacial earthquakes lack coherent signal at short periods even at GLISN seismometers located within 100 km of glacier termini.

In this study, we explore an approach in which we incorporate information from non-seismic data to elucidate the character of the force-time history of a calving iceberg that generates a glacial earthquake. Analog experiments of iceberg calving in the laboratory have proven valuable in advancing understanding of buoyancy-driven calving (Cathles et al., 2015; Murray, Nettles, et al., 2015). In laboratory experiments conducted by Cathles et al. (2015), iceberg calving is simulated by capsize of a plastic block within a water-filled tank (Figure 3). Sensors located within the "glacier" terminus record force and pressure timeseries throughout the capsize of the analog iceberg, thereby providing observations of the time-varying horizontal and vertical forces applied by a calving iceberg

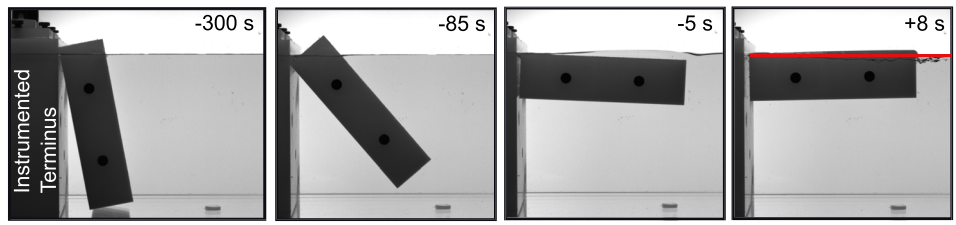

Figure 3. Photographs taken at four points in time during a tank experiment. The iceberg-analog block shown here has an aspect ratio of 0.28. Time values printed in the upper right of each panel are relative to the time the iceberg-analog block first reaches horizontal ($t = 0$ s; not shown). The thin red line in the fourth panel shows a horizontal reference for this experiment. The force and pressure histories recorded during this experiment (Experiment 5) are shown in Figure 5.

to the solid Earth, in a laboratory setting. When scaled up to glacier dimensions, the force histories recorded in laboratory experiments closely match the duration and character of GPS-derived observations of glacier displacement during calving (Murray, Nettles, et al., 2015). The recorded force histories are also similar to force histories calculated in numerical simulations (Sergeant et al., 2018). The consistency between the force histories observed in laboratory experiments, GPS observations, and numerical-modeling results suggests that the laboratory experiments, while not real Earth observations, likely capture the critical aspects of the force history at the glacier front during generation of a glacial earthquake. In addition, seismic-magnitude values, M_{CSF}, calculated for the tank events using the same seismic modeling approach and 50-s boxcar source model used in standard analysis of glacial earthquakes are in close agreement with results for real glacial earthquakes (Figure 2).

We employ an existing set of laboratory experiments of iceberg calving (Burton et al., 2012; Cathles et al., 2015) to construct new models of the seismic source time function for use in glacial-earthquake waveform modeling. This is the first introduction of such constraints into seismic modeling of glacial earthquakes. We assess the ability of source models of this type to return improved estimates of source parameters, using both seismograms from synthetic events and observed glacial earthquakes. We explore the relationship between iceberg size and seismic magnitude, and consider additional metrics of seismic magnitude beyond M_{CSF}, including peak force and peak momentum. By incorporating laboratory-based constraints into seismic analysis, we demonstrate the utility of a more sophisticated, physics-based source model for glacial earthquakes, and lay out a framework for future work to further advance glacial-earthquake modeling.

2. Background

2.1. Estimation of the Seismic Source

The time-varying force exerted by a calving iceberg in the direction opposite its acceleration is similar in geometry to that generated by a landslide mass accelerating downhill. Glacial earthquakes, like landslides, can be modeled using a centroid-single-force (CSF) approach (Ekström et al., 2003; Kawakatsu, 1989). The CSF technique is closely related to the CMT technique (e.g., Dziewonski et al., 1981) used to model the sources of tectonic earthquakes. Ground motion recorded at a seismic station depends on the source that generates the waves and on the Earth structure through which the waves travel. Ground motion u in direction k recorded at a seismic station at location $\mathbf{r}$ can be written

$$u_k(\mathbf{r}, t) = \sum_{i=1}^{N} \Psi_{ik}(\mathbf{r}, \mathbf{r_s}, t) * S_i(t) \cdot f_i \tag{1}$$

where the $*$ denotes convolution, and the Green function Ψ describes the predicted seismogram generated by a point force $\mathbf{f}$, acting at location $\mathbf{r}_s$, for a given model for Earth structure. In the CMT approach, the vector f_i contains the amplitudes of the six independent elements of the moment-rate tensor, and $N = 6$. In CSF analysis f_i contains the amplitude of a point force acting in direction i, and $N = 3$, with the summation over the three orthogonal components of the force vector (South, East, and up). The time history of the seismic source is represented by the source time function $S_i(t)$. In most CMT and CSF applications, $S_i(t) = S(t)$, for all i, such that the shape of the time function is the same for each component of the moment tensor or force vector.

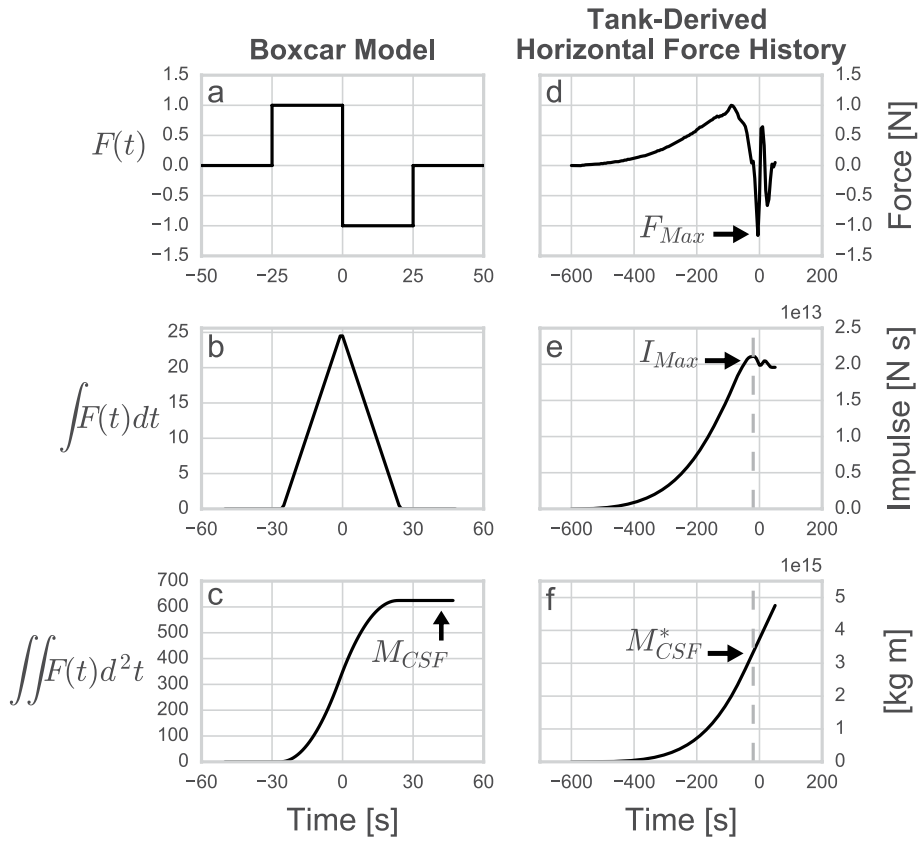

Figure 4. Force histories and integrated quantities for (a–c) the 50-s boxcar model and (d–f) laboratory Experiment 5 (Figure 5). The first row in each column shows force histories $F(t)$. F_{Max} in panel (d) identifies the maximum force, taken in an absolute sense, for this particular force history. The second row in each column shows the integral with respect to time of each force history, the impulse history $I(t) = \int F(t)dt$. For the boxcar model, the maximum impulse value occurs at $t = 0$ s. In panel (e) the time of the maximum impulse value (I_{Max}) for this particular force history is identified by the gray dashed line. The third row shows the second integral with respect to time of each force history, $M_{\mathrm{CSF}}(t) = \iint F(t)d^2t$. For the boxcar model, the twice-integrated force history reaches its final value at $t = 25$ s and then remains constant; this constant value is referred to as M_{CSF} in glacial-earthquake literature. For the tank-derived force history, which does not integrate to zero, we choose in this study to evaluate the twice-integrated force history at the time of the maximum impulse value, denoted by the gray dashed line, and we refer to this value as M_{CSF^*}.

The formulation of the ground-motion equation is thus similar for CMT and CSF analysis, and accurate ground-motion prediction relies upon both a robust model of Earth structure and a model of the source time function. A point-source approximation in space is adequate for long-period data where the wavelength is much greater than the spatial extent of the source. This condition is met both for glacial earthquakes and for moderate-sized tectonic earthquakes in the 50–150 s period band typically used (Ekström et al., 2012) in analysis of events of this size. However, the function $S(t)$ is prescribed in both CMT and CSF analysis because, in both cases, these data have insufficient sensitivity to the shape of the source time function to allow its independent retrieval.

With models for both structure and source defined, the inverse problem can be solved for f_i. In practice, the source time and location are not precisely known upon event detection. Therefore, inversion for the elements of the source, f_i, the event time, and location is conducted simultaneously, using a linearized approach (e.g., Dziewonski et al., 1981; Ekström et al., 2012). In our work, we follow the implementation of Ekström et al. (2012).

For tectonic earthquakes, the source variation with time is described by the moment-rate function. In CSF analysis, the force history or its integral is used as the source time function, $S(t)$. A simple, double-boxcar force model of the seismic source of glacial earthquakes (Figure 4a) has been used in analysis of all events in the glacial-earthquake catalog to date (Olsen & Nettles, 2017, 2019; Tsai & Ekström, 2007; Veitch & Nettles, 2012). This model specifies a 50-s-long, anti-symmetric source time function that represents a constant force applied to the Earth

for 25 s as the iceberg accelerates away from the glacier terminus, followed by a 25-s constant force of equal amplitude and opposite sign as the iceberg decelerates (Figure 4a).

The boxcar model satisfies the requirement that momentum be conserved, and has been found to produce good fits to available data. Given a constant mass, the first integral of the CSF force history with respect to time represents the momentum history of the moving mass, also known as the impulse (Figure 4b), and the twice-integrated force history can be interpreted as the product of the mass and the distance over which acceleration occurs. The value to which the mass-distance product converges (the zero-frequency value) has been termed the centroid-single-force magnitude, M_{CSF} (Figure 4c). The M_{CSF} value is analogous to the seismic moment for a tectonic earthquake, in the sense that it is a summary measure of earthquake size obtained when the event has terminated. As with tectonic-earthquake studies, zero-frequency data are not necessary to retrieve an estimate of this "zero-frequency" value for glacial earthquakes. Instead, in both tectonic- and glacial-earthquake studies, an accurate model of the seismic source allows for accurate retrieval of event size.

2.2. Constraints on the Shape of the Glacial-Earthquake Force History

2.2.1. Analog Laboratory Experiments and GPS Observations of Iceberg Calving

Though field observations of buoyancy-driven calving are sparse, insight has been gained through analog studies simulating iceberg calving with a plastic block in a water-filled tank (Figure 3; Amundson et al., 2012; Burton et al., 2012; Cathles et al., 2015). During capsize of an analog iceberg, sensors located within the tank wall record time series describing either the force or the pressure changes generated by iceberg rotation and hydrodynamic effects (Figure 5; Cathles et al., 2015). High-rate photographic imagery allows synchronization in time of the force and pressure records for a given iceberg. Additional details of the laboratory setup are given by Burton et al. (2012) and Murray, Nettles, et al. (2015).

Force and pressure histories recorded in the lab can be scaled up to glacier dimensions when the ratio between iceberg height in the field and in the laboratory is known (Amundson et al., 2012; Burton et al., 2012; MacAyeal et al., 2011). Scaled-up laboratory force and pressure records predict well the glacier deflection that is observed to occur during iceberg calving (Murray, Nettles, et al., 2015). Furthermore, M_{CSF} values calculated from synthetic seismograms generated from these scaled-up laboratory force records are in close agreement with M_{CSF} values estimated for true glacial earthquakes (Figure 2). The experimental data thus appear to provide a robust analog with which to investigate details of the time-varying force generated during iceberg capsize, as well as the relationship between iceberg size and force magnitude.

In this study, we focus on bottom-out buoyancy-driven calving, for which capsize occurs spontaneously when a tall, narrow plastic iceberg is placed vertically within the water column against one end of the tank (Figure 3). Force and pressure histories recorded for analog icebergs of four different aspect ratios (Cathles et al., 2015) and scaled up to a variety of iceberg heights observed in the field (Murray, Nettles, et al., 2015) are shown in Figure 5. The first ~600 s of each horizontal-force history recorded during tank experiments shows a gradual increase in up-glacier force amplitude, which we define as a positive force, followed by a more rapid decrease (Figure 5). This part of the force history, during which the horizontal-force values are positive (gray-shaded portions of panels in Figure 5), is interpreted as the glacier response to seaward iceberg acceleration during capsize (Murray, Nettles, et al., 2015). The maximum up-glacier force is labeled "a" in the upper-left panel of Figure 5. Following this acceleration phase of the force history, each of the laboratory-derived horizontal-force histories contains a rapid force reversal to a down-glacier (negative) force lasting approximately 20 s ("b" in the upper left panel of Figure 5). We interpret this part of the force history as the glacier's response to rapid iceberg deceleration. The deceleration likely results from the combination of a reduced buoyancy force, as the iceberg nears horizontal and no longer has significant mass out of isostatic equilibrium in the water column, and the resisting force generated by water in the fjord slowing the iceberg's forward motion. A second up-glacier force peak ("c" in the upper left panel of Figure 5) is observed following the force reversal. This up-glacier force is ~10 s long and reaches between ~30% and 100% of the amplitude of the earlier up-glacier force ("a"). Based on videos from the tank experiments (Burton et al., 2012; Cathles et al., 2015), this part of the force history appears to be generated by the iceberg rotating past horizontal so that part of the face of the iceberg that previously formed the iceberg's top surface comes in contact with the glacier's calving face (see fourth panel, at +8 s, in Figure 3). Such over rotation is also observed in some high-frame-rate images of buoyancy driven calving in the field (e.g., James et al., 2014).

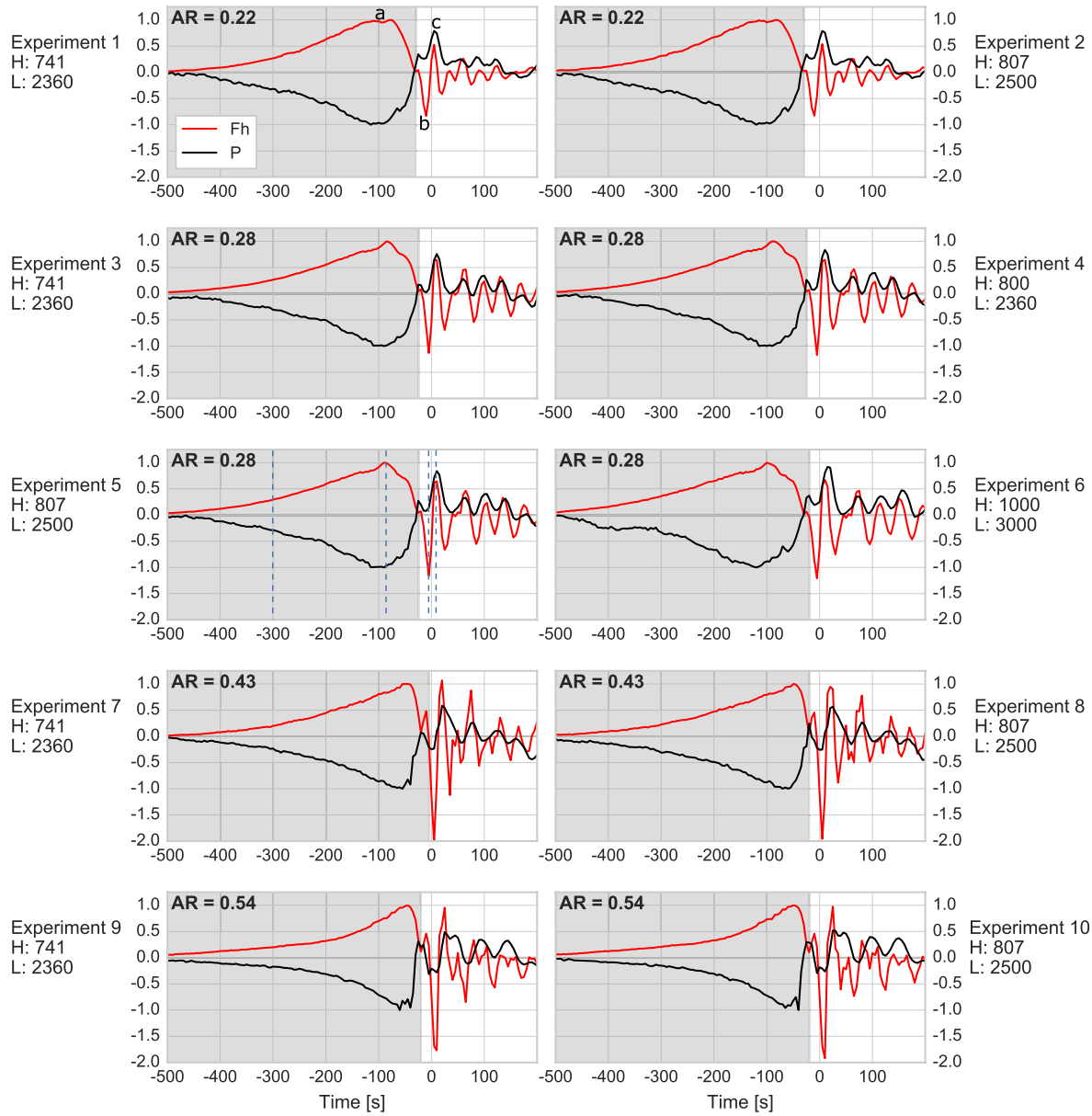

Figure 5. Histories of (red) horizontal force and (black) pressure for the 10 laboratory experiments used as seismic sources in this study. Gray shading identifies the part of the time series referred to in the text as the "left-hand side"; white background identifies the part of the time series referred to as the "right-hand side". Each force and pressure history is normalized by the maximum value of the timeseries within the gray-shaded region. Iceberg aspect ratio (AR) is shown for each experiment, and scaled-up dimensions for each analog iceberg are given below the Experiment number. H: iceberg height in m; L: iceberg length in m. Positive vertical-axis values represent horizontal force in the up-glacier direction, or increased pressure. Time = 0 in each experiment represents the time at which the capsizing iceberg first reached horizontal. "a", "b", and "c" in the top left panel refer to parts of the horizontal-force histories discussed in the text. The blue dashed lines shown for Experiment 5 denote the times of the photographs of this experiment shown in Figure 3.

The pressure records are out of phase with the horizontal forces during the first ~600 s of the tank time series (gray-shaded portions of panels in Figure 5), showing a pressure decrease as the horizontal up-glacier force increases. A pressure decrease in the water column results in a vertical force on the solid Earth, oriented upwards. During this acceleration phase of the force history, the up-glacier horizontal force and negative pressure values result in an up-glacier, upward force. After the horizontal force crosses zero, the pressure records become generally in phase with the horizontal force (white portion of panels in Figure 5). At the time of the largest down-glacier horizontal force ("b"), pressure deviations are near zero. During up-glacier force peak "c", pressure excursions are positive, resulting in a total force oriented downward and up glacier. The remainder of the horizontal force

and pressure time series for a given tank experiment are in phase, and are not coherent between experiments. This final part of the time series is attributed to water waves oscillating in the experimental tank (Burton et al., 2012; Cathles et al., 2015). In the experimental set-up, measures are taken to damp seiche modes following iceberg capsize (e.g., Murray, Nettles, et al., 2015), but waves are not fully eliminated.

The geometry of forces from the laboratory experiments–dominated by an up-glacier, upward force reversing to an initially down-glacier, downward force–is consistent with that estimated for the majority of the 450 glacial earthquakes that have been analyzed, and which occurred at 15 glaciers around Greenland over more than two decades. This consistency, and an initial seismic analysis of scaled-up tank data conducted by previous authors (Murray, Nettles, et al., 2015), suggest that the laboratory data accurately represent the forces that generate the seismic signal.

On-glacier GPS data recorded during calving (Murray, Nettles, et al., 2015) have similar characteristics to the force histories seen in all bottom-out laboratory experiments. GPS instruments deployed on Helheim Glacier in East Greenland captured glacier motion during multiple bottom-out buoyancy-driven calving events in 2013 (Murray, Nettles, et al., 2015). During each calving event, instruments located on ice within ∼1 km of the terminus recorded the front of the glacier being displaced ∼10 cm up-glacier for ∼300 s during the first stages of iceberg calving (Murray, Nettles, et al., 2015). The direction of horizontal-displacement data then reverses as the glacier front moves through and forward of its pre-calving position before returning to equilibrium. The shape and timing of these displacement records are in close agreement with the upscaled horizontal-force records from the laboratory experiments (Murray, Nettles, et al., 2015). The vertical-component GPS observations show the glacier terminus drawn down and then uplifted, again with the shape and timing of the records in agreement with the pressure drop and increase recorded in the laboratory experiments (Murray, Nettles, et al., 2015). In glacier fjords, ice mélange serves to partially damp water waves (e.g., Amundson et al., 2010), and oscillations like those following peak "c" (Figure 5) are not observed in glacier GPS data (Murray, Nettles, et al., 2015).

In the following text, we refer to the first ∼600 s of the source as the left-hand side, from first signal onset to the time of the first zero crossing of the horizontal force (gray-shaded portions of panels in Figure 5). We refer to the time period beginning at the first force zero crossing and including the ∼20 s down-glacier force as well as the lower-amplitude up-glacier force that follows as the right-hand side of the source (white portions of panels in Figure 5). All figures begin at −500 s, rather than −600 s, for ease of viewing.

2.2.2. Numerical-Modeling Results

Numerical simulations of the forces generated by buoyancy-driven iceberg capsize against a glacier terminus show key characteristics of both the laboratory and field observations. Using a 2D 'finite-element approach', Sergeant et al. (2018) modeled the horizontal contact force between an iceberg and a glacier terminus, including an approximation of hydrodynamic drag forces acting on the glacier-terminus system. Sergeant et al. (2018) calculated the horizontal force generated during the iceberg-acceleration phase of calving, from the time an iceberg begins rotation through the time the iceberg loses contact with the calving face (i.e., the part of the force histories shaded gray in Figure 5), and predicted rotation durations of 100–200 s for icebergs with geometries like those considered in this study. The shapes of the predicted force time series are similar to those observed in the laboratory and inferred from GPS data.

With increasing aspect ratio, the force histories calculated by Sergeant et al. (2018) display a steeper slope as they approach peak force, an effect also seen in laboratory results (Figure 5). Because the model of Sergeant et al. (2018) describes force values only during the time the iceberg is in contact with the terminus, it does not capture the iceberg-deceleration phase of the source that is recorded in laboratory and field observations (e.g., "b" in Figure 5). It therefore does not predict any down-glacier force. However, the agreement of the numerical-model results with the tank experiments and GPS observations supports the reliability of the laboratory results, and the possibility of using this information for better-informed inverse modeling of recorded seismic data.

2.2.3. Limitations in Knowledge

The laboratory experiments, GPS observations, and numerical-modeling results provide a far more detailed picture of the time history of forces acting on the solid Earth during calving than was available previously. However, some important limitations remain. The available laboratory experiments measure force and pressure on the wall of the experimental tank that represents the calving face (Figure 3), but not on the rest of the system, including

the fjord floor and walls. GPS observations are limited to the glacier surface, and internal deformation must be inferred. The numerical experiments provide a force history only through the time of loss of iceberg contact with the calving face and so do not describe forces active during the full rotation of the iceberg or during its subsequent motion away from the terminus.

Details of the force history after the time of force reversal (i.e., during the white-shaded, "right-hand" side of the force histories shown in Figure 5) are particularly poorly constrained. Glacier displacement records from on-ice GPS instruments (Murray, Nettles, et al., 2015) become more difficult to interpret after the rapid force reversal, in part due to glacier acceleration immediately following buoyancy-driven calving (Nettles et al., 2008). Laboratory records become less coherent after the iceberg first reaches horizontal because of water waves in the tank. Available numerical models do not describe this time period. None of the records demonstrate, on their own, conservation of momentum. It is likely that momentum is transferred to the tsunami that propagates away from the calving front following glacial earthquakes. However, only a few studies (e.g., Heller et al., 2019; MacAyeal et al., 2011) have addressed the characteristics of iceberg-related tsunamigenesis, and investigation of that phenomenon is beyond the scope of the current study.

Despite these limitations, the detail captured in the laboratory results and supported by GPS data and numerical models suggests the potential for great improvement compared with the boxcar model (Figure 4a) used previously. We therefore proceed using the laboratory data as the basis for an exploration of improved models of the glacial-earthquake source time function.

3. Methods

We construct synthetic seismograms using as the "true" source time functions the force and pressure histories recorded in laboratory experiments and scaled up to natural glacier dimensions. We then treat these synthetic seismograms as data, and invert for glacial-earthquake source parameters using the same, CSF, approach as applied in previous studies. In these inversions we use various source time functions, $S(t)$, and evaluate the accuracy of the source parameters obtained with each type of time function.

3.1. Construction of Synthetic Seismograms

Calculation of synthetic seismograms requires the Green functions for a specified Earth structure, the amplitudes of the forces acting on the Earth at the source location, and a specified time history for those forces (Equation 1, Section 2.1). We calculate seismograms using normal-mode summation in the preliminary reference Earth model (PREM; Dziewonski & Anderson, 1981) to a minimum period of 30 s. Seismograms are calculated for a synthetic array of 11 stations located at epicentral distances between 10° and 70° from the source and equally spaced 30° apart in azimuth. The station distribution is chosen to represent the limited range of observing distances and azimuths available for analysis of glacial earthquakes at Greenland glaciers.

In this proof-of-concept study we restrict our analysis to noise-free synthetic seismograms. We anticipate the effect of noise will be small, based on the signal-to-noise ratios observed in the twenty-year glacial-earthquake catalog. In addition, Olsen and Nettles (2019) demonstrated that robust source parameters can be recovered for even very small glacial earthquakes with low signal-to-noise ratios.

To represent the "true" source time function, we use the force and pressure histories shown in Figure 5, recorded during experiments with analog icebergs having along-flow-width versus height aspect ratios of 0.22, 0.28, 0.43, and 0.54, similar to the range of aspect ratios observed in the field for capsizing icebergs (Amundson et al., 2010). Laboratory force and pressure histories were scaled up to field dimensions (Burton et al., 2012; Murray, Nettles, et al., 2015) for iceberg heights ranging from 741–1,000 m, cross-glacier lengths ranging from 2,360–3,000 m, and along-glacier widths ranging from 160–430 m, consistent with observed dimensions of icebergs from Jakobshavn Isbræ and Helheim Glacier (e.g., Murray, Selmes, et al., 2015; James et al., 2014; Walter et al., 2012). Two to four different iceberg sizes are considered for each aspect ratio.

We smooth the scaled-up force and pressure data using a 5-s moving average to remove high-frequency instrument noise associated with the laboratory recordings, and remove the non-zero mean background signal using 350 s of each record before signal onset. To convert pressure records to vertical-force values we multiply each pressure time series by the basal area of the unrotated iceberg used for each experiment, following Murray,

Nettles, et al. (2015). This conversion represents a simplification compared to the true ice-water-rock system, but produces a ratio of vertical to horizontal forces similar to that observed for natural glacial earthquakes. In all experiments, $t = 0$ is defined as the time at which the capsizing iceberg first reaches horizontal. To generate each seismic source we trim the records to begin at $t = -600$ s, which is the approximate time at which the signal first deviates from zero. Following iceberg capsize, water waves oscillate in the tank and dominate both force and pressure records to an extent not expected in the field due to damping from ice mélange (e.g., Amundson et al., 2010). We truncate the right-hand side of each record at $t = +50$ s, which allows us to include source signal consistent in character across experiments, while omitting the majority of later water-driven oscillations.

We parameterize the shape of each horizontal and vertical input force independently using a set of isosceles triangles with durations of 10 s, fixed to overlap one another by 50%, to produce an accurate representation of the time series. We specify an initial westward orientation for all horizontal forces, and an initial upwards orientation for all vertical forces, an arbitrary choice that simplifies bookkeeping. The horizontal along-glacier and vertical force functions are included as the terms $S_i(t)$ in the ground-motion equation; the horizontal cross-glacier term is identically zero.

3.2. Inversion Procedure

We bandpass filter the synthetic seismograms calculated in Section 3.1, transformed to ground velocity, to the period band 50–150 s, consistent with standard analysis of glacial earthquakes. We invert each set of input seismograms using the analysis approach employed in previous glacial-earthquake studies (e.g., Ekström et al., 2003; Olsen & Nettles, 2017; Tsai & Ekström, 2007; Veitch & Nettles, 2012), with the exception that we specify a wide variety of time functions $S(t)$ in our inversions, rather than using only the 50-s boxcar employed in previous studies. That is, for each synthetic glacial earthquake, we perform multiple inversions, each with a different specified time function $S(t)$.

For most experiments, wave propagation is calculated using PREM (Dziewonski & Anderson, 1981), the same Earth model used to calculate the synthetic "data" seismograms, a strategy that allows us to isolate the effects of the source time function on recovery of earthquake parameters. However, the Earth's three-dimensional seismic velocity structure is not perfectly known, and, in inversions of natural earthquake data, some misfit to the seismograms will result from differences between the true Earth structure and that specified for calculations of model seismograms. We therefore also perform some experiments, using a standard 50-s boxcar time function, in which the Earth model for inversion is described by the phase-velocity maps of Ekström (2011). The difference between the true structure in this case (PREM) and that used for inversion (the laterally varying phase-velocity maps) is far greater than that expected between the real Earth and high-quality models of Earth structure like those used in previous CSF inversions of glacial earthquakes (e.g., Olsen & Nettles, 2017), and our experiment thus represents an upper bound on the effect of mismodeled Earth structure.

Inversion outputs in all cases are assessed using standard criteria including the fit to the data, inversion stability, and time and location shift (Ekström et al., 2012), as well as recovery of the input parameters.

3.3. Construction of Model Source Time Functions

As an alternative to the 50-s boxcar time function used previously, we construct a set of models representing the earthquake force history with varying degrees of complexity. The simplest models retain the boxcar shape (Figure 4a), with a force history that integrates to zero, but we specify a variety of source durations ranging from 10–400 s.

We construct a second set of models using simplified representations of the shape of the force histories recorded in the laboratory experiments. Because GPS observations, laboratory observations, and numerical-modeling results are in general agreement on the shape and duration of the left-hand side of the glacial-earthquake source, we construct the left-hand side of most of these models from the average shape of this part of the tank experiments: We normalize the horizontal force histories recorded in eight of the tank experiments (two for each of the four aspect ratios considered), align them on the first zero-crossing time of the force history (approximately $t = -20$ s), and calculate the mean of the time series.

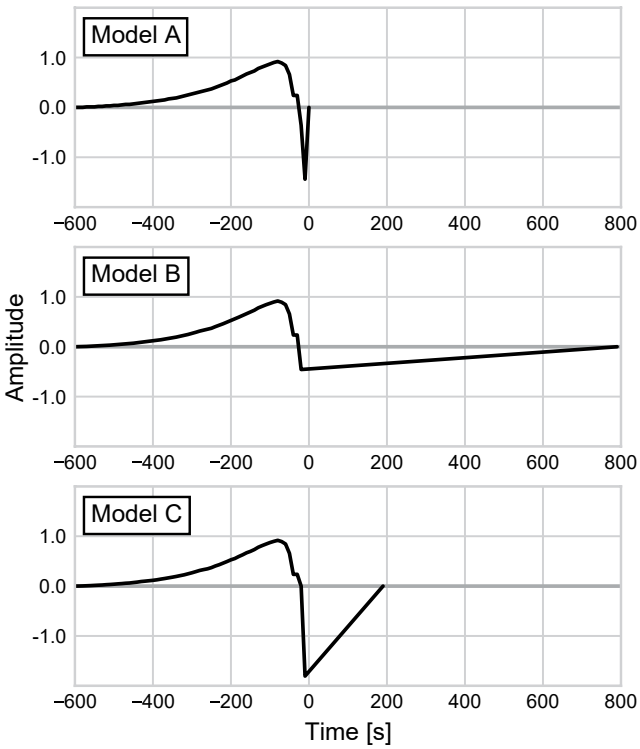

Figure 6. Representative source-time-function models $S(t)$ used in this study. Left-hand side of each force history, from $t = -600$ s to the first zero crossing, is calculated by aligning the normalized horizontal force histories recorded during eight laboratory experiments on their zero-crossing time and taking the average. The portion of Model A after the zero-crossing time is also taken from the laboratory average. The portion of Model B after the zero-crossing time is constructed so that the maximum-force value is one half of the maximum value on the left-hand side, and the areas of the two sides are equal. The portion of Model C after the zero-crossing time is constructed so that the maximum-force value is twice the maximum value on the left-hand side, and the areas of the two sides are equal.

A second robust feature observed in all three non-seismic datasets is the rapid force reversal from up-to down-glacier orientation. Because seismic waves are efficiently generated by rapid force changes, we expect this feature may control most of the seismic signal recorded for glacial earthquakes. We therefore include a rapid force reversal in the majority of models tested in this study.

Additionally, GPS observations and laboratory results show vertical force histories with shapes generally similar to the horizontal force histories up to the time of the rapid force reversal (Murray, Nettles, et al., 2015). We therefore simplify construction of models in this study by specifying vertical and horizontal force functions that have the same shape. That is, $S_i(t) = S(t)$ for all force components.

From the large suite of models we construct, we choose three representative models to discuss in detail (Figure 6). We refer to these as Models A, B, and C. The left-hand side of Model A is constructed using the tank-average shape described above. The right-hand side of Model A is constructed to include the rapid force reversal and ∼20 s of the down-glacier force taken from the tank-averaged time series. Model A does not integrate to zero (Figure 6). The left-hand side of Model B is constructed using the tank-average shape, and the right-hand-side is constructed as a triangle with area equal to that of the left-hand side. The maximum force on the right-hand side of Model B is one half the value of the maximum force on the left-hand side (Figure 6), similar in amplitude to that observed in tank experiments 1 and 2 (Figure 5). Model C is constructed in the same way as Model B, but the right-hand-side triangle has a maximum-force amplitude twice that of the maximum-force amplitude on the left-hand side (Figure 6), similar to the amplitudes observed in tank experiments 7–10 (Figure 5). Models B and C integrate to zero.

3.4. Analysis of Inversion Results

In addition to assessing how well the input location, time, and geometry of the true source are recovered in our inversions, we evaluate several measures of earthquake size for each event. Because the tank-derived force histories we use to generate the synthetic seismograms do not integrate to zero, the input twice-integrated force history does not reach a constant value (Figure 4), and a zero-frequency M_{CSF} value is not well defined. The non-zero integral of the force history indicates that momentum is not conserved in this simplified system. As noted earlier (Section 2.2.3), the laboratory force measurements are made on the calving face; momentum must be transferred to other parts of the tank setup, in the same way that momentum is expected to transfer to other parts of the fjord in a natural glacier setting.

We choose to evaluate the tank-derived impulse function (Figure 4e) and the twice-integrated source time function (Figure 4f) at the same point in time, when the horizontal force first crosses zero and when the impulse function reaches its maximum value (Figure 4d). We refer to the value of the twice-integrated force function reported at the time of maximum impulse (Figure 4f) as M_{CSF^*} to distinguish it from the zero-frequency M_{CSF} value illustrated in Figure 4c. We also consider a third metric for glacial-earthquake size, maximum force, defined as the maximum absolute value of the force history (e.g., Figure 4d). For some tank experiments, this value occurs at point (a), on the left-hand side of the force history, while for others it occurs at point (b), on the right-hand side (Figure 5).

4. Results

Results from our inversions of seismograms calculated using the force and pressure histories of Figure 5 show that earthquake locations and force azimuths are very well recovered using all source models tested, while recovery of force amplitude and other earthquake-size metrics depends strongly on the source model specified, as described further below and illustrated in Figures 7–9.

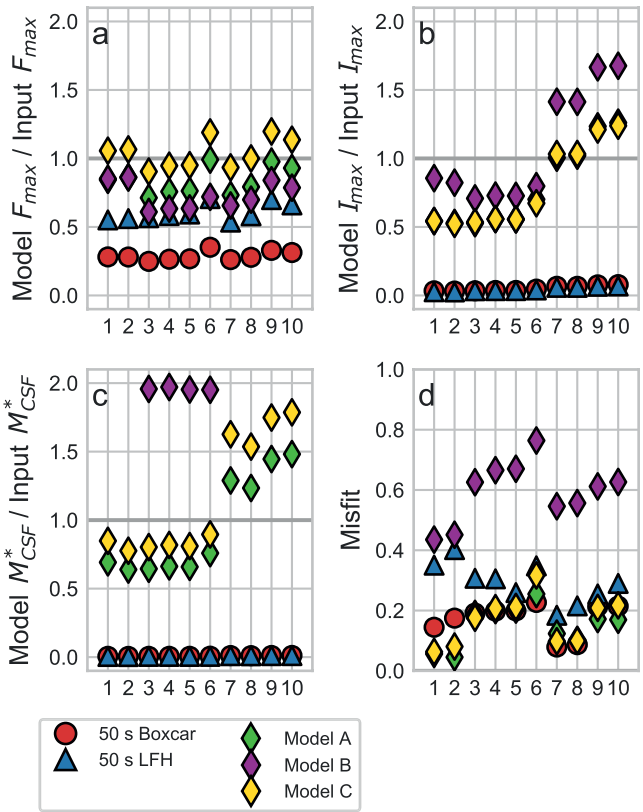

Figure 7. Recovery of source parameters for five models discussed in the text. Event numbers (horizontal axes of all panels) refer to the laboratory experiments shown in Figure 5. Panel (a) shows a comparison of maximum-force results (F_{Max} identified as in Figure 4d). Panel (b) shows a comparison of maximum-impulse results (I_{Max} identified as in Figure 4e). Panel (c) shows a comparison of M_{CSF^*} results (M_{CSF^*} identified as in Figure 4f). Panel (d) shows inversion misfit values for each model, where the misfit is defined as the residual variance between input seismograms and those predicted from inversion results. Some symbols for Model A plot beneath symbols for Model C in panels (a) and (b), and some data points for Model B in panel (c) plot beyond the upper limit of the figure.

The majority of event latitudes (98%) are recovered to within 2.5 km, and all longitudes to within 6 km, regardless of the selected source model. This range of recovered location values is well within the location uncertainty typical for glacial earthquakes analyzed using the traditional boxcar-model approach (15–30 km; Veitch & Nettles, 2012). Recovered force azimuths never deviate from the input values by more than 1°.

The orientation of the applied force with respect to horizontal, or plunge, of the input model varies with time, while the inversion procedure produces a single estimate of the plunge because the specified shape of the source time function $S(t)$ is the same in the vertical and horizontal directions. However, the shallow plunge values recovered using all models in this study (0–36°) are consistent with plunge values (3–35°) for the left-hand side of the input force histories, as well as with the plunge values reported in the glacial-earthquake catalog (Olsen & Nettles, 2017; Tsai & Ekström, 2007; Veitch & Nettles, 2012).

The dependence of the recovery of input force amplitudes on the source model is illustrated in Figure 7. Inversions conducted using a 50-s boxcar-shaped source model (Figure 4a) return maximum-force values between 0.25 and 0.33 of the true maximum-force values of the input source (Figure 7a). The corresponding maximum impulse and twice-integrated force-history values for the boxcar model (Figures 7b and 7c) are ~0.05–0.01 those of the true values, primarily because the duration of this model is less than 10% that of the input source. The 50-s boxcar model produces very good fits to the tank-derived waveforms, with residual variance ("misfit") values of 0.1–0.2 (Figure 7d). We also experiment with boxcar-shaped source models with durations ranging from 10–400 s (not shown). Boxcar models with durations longer than 50 s generally recover maximum-force, maximum-impulse, and twice-integrated force-history values somewhat better than the 50-s model, but fit the input seismograms less well. The 400-s model provides the best recovery of maximum force (0.3–0.4 of the true values), maximum impulse (0.3–0.9 of the true values), and M_{CSF^*} values (0.5–1.3 of true values) of the boxcar models we test, but produces misfit values as high as 0.5.

Inversions conducted using Models A, B, and C recover maximum-force values better than any of the boxcar sources, including the standard 50-s boxcar (Figure 7a). Model C produces maximum-force values closest to input values: 0.9–1.2 of the true values. Model A also performs very well, producing maximum-force values 0.7–1 of the true values. Model B performs less well, producing maximum-force values 0.6–0.9 of the true values. The recovery of maximum-impulse values is dependent on iceberg aspect ratio for all three models (Figure 7b). For experiments using icebergs with aspect ratios of 0.22 or 0.28 (Experiments 1–6), Models C and A produce maximum-impulse values 0.5–0.7 of the true values; Model B produces maximum-impulse values 0.7–0.9 of the true values. For experiments using icebergs with larger aspect ratios of 0.43 or 0.54 (Experiments 7–10), Models C and A recover maximum-impulse values that are 1.0–1.3 of the true maximum-impulse values; and Model B recovers 1.4 to 1.7 of the true values. The recovery of M_{CSF^*} values also depends on iceberg aspect ratio, with values underpredicted for the smaller (0.22, 0.28) aspect ratios and overpredicted for the larger aspect ratios (0.43, 0.54) for both Models A and C (Figure 7c). Inversions using Model B produce M_{CSF^*} values that exceed the true values (1.95–4.47) for all 10 experiments.

Inversions using Models A and C result in low misfit values, with model seismograms that fit the input seismograms well. Experiments using Model A produce misfit values ranging from 0.05–0.25, with an average value of 0.15 (Figure 7d). Experiments using Model C produce misfit values ranging from 0.06–0.32, with an average of 0.17. For both Model A and Model C, the fit to the data achieved is comparable to that for the 50-s boxcar model. Waveforms generated using Model B are dominated by longer periods than the input seismograms, and fit the data less well, with misfit values ranging from 0.44–0.76.

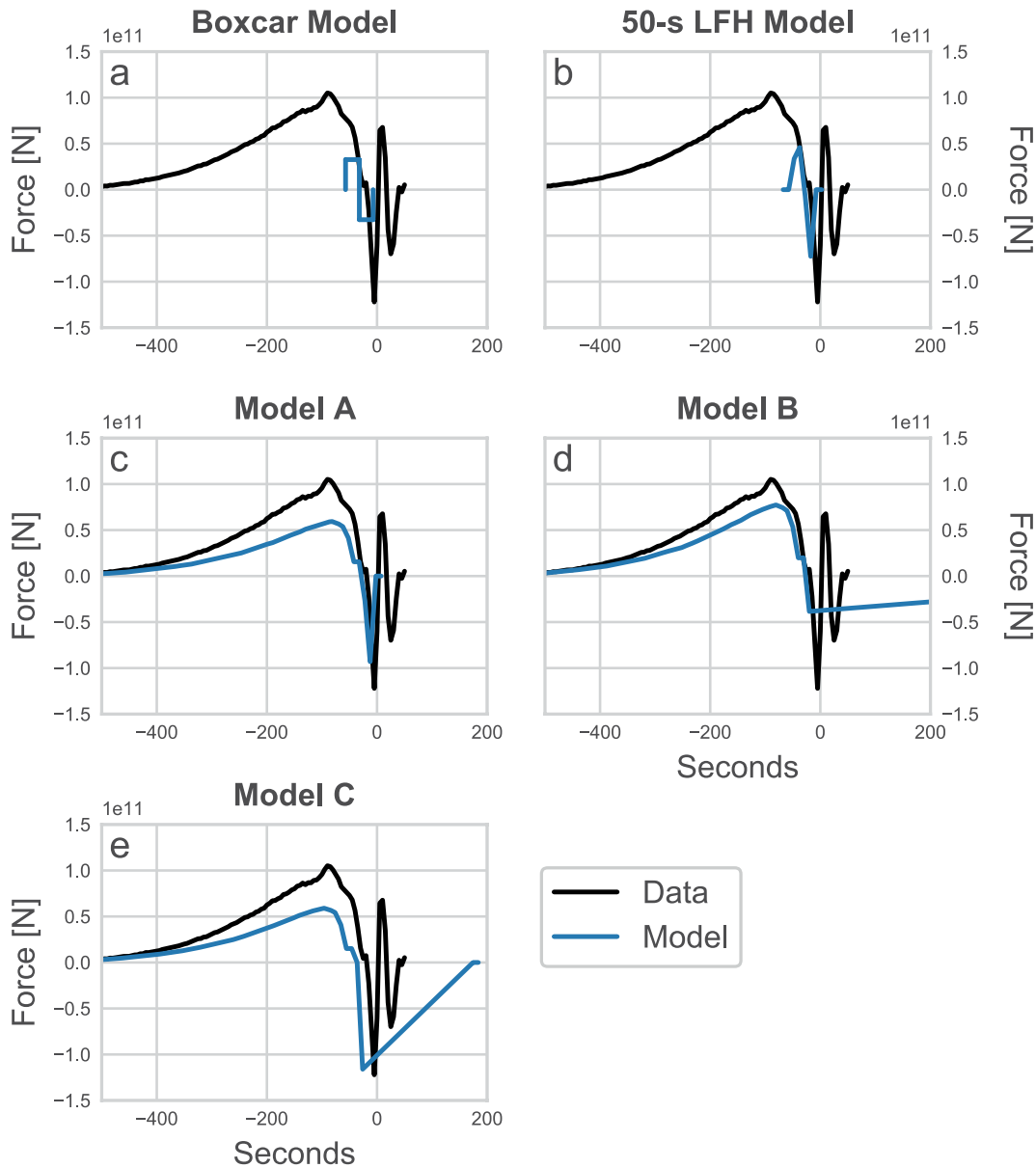

Figure 8. Horizontal-force data from Experiment 5 (aspect ratio: 0.28; Figure 5), shown with the east-west components of the horizontal-force results recovered using the five models described in this study. Model B extends beyond the edge of the figure, to ~800 s. The blue lines in each panel are not fit to the black lines, but show the source time functions $S(t)$ with scaling and time shifts recovered from inversion.

Results for experiments using time functions with shapes similar to Models A–C but with a range of durations (from 20–1,500 s) produce results consistent with those from Models A–C. Event locations and force orientations are recovered very robustly, and recovery of maximum-force, maximum-impulse, and M_{CSF} values follows the behavior illustrated in Figure 7 and described above.

The recovery of source parameters is only minorly affected by the use of different Earth models for generation of input seismograms (PREM) and for inverse waveform modeling (GDM52; Ekström, 2011). Although the imperfect representation of Earth structure resulting from the difference in the two Earth models produces systematic biases in predicted surface-wave phase–larger than those expected for any reasonable level of Earth noise–recovery of earthquake geometry and size is degraded little. In these experiments, in which a 50-s boxcar function is

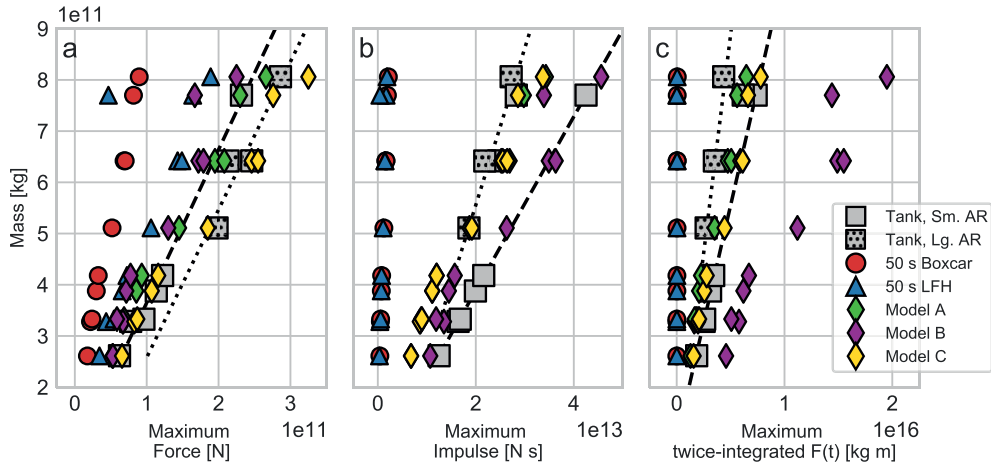

Figure 9. Measures of seismic magnitude versus iceberg mass for tank-derived data and model results. Mass values are from scaled-up analog iceberg dimensions. Laboratory maximum force, maximum impulse, and twice integrated $F(t)$ values (M_{CSF^*}), shown by gray squares (stippled and solid), are measured from tank data as shown in Figure 4 and described in Section 3.3.4. Black dashed line indicates best fit to the six laboratory experiments (Tank, Sm. AR) with small aspect ratios (0.22 and 0.28). Black dotted line indicates best fit to the four laboratory experiments (Tank, Lg. AR) with large aspect ratios (0.43 and 0.54). Colored symbols show values of F_{max}, I_{max}, and M_{CSF} retrieved by seismic modeling of the waveforms calculated for each experiment. With perfect recovery, the colored symbols would lie on top of the gray squares.

used both as the true source model and as the function $S(t)$ for inversion, azimuth values are recovered to within 3° and plunge values to within ∼5°.

5. Discussion

Our experiments with synthetic glacial-earthquake data show excellent recovery of earthquake geometry and location using the CSF approach, with all of the source-history models we test: the 50-s boxcar; Models A, B, and C; and variations on these models with longer and shorter durations and different ratios of force amplitudes between the left- and right-hand sides of the force history. As anticipated, results from the 50-s-boxcar model underestimate the amplitude of the source. Despite the fact that the best-performing models, A and C, are highly simplified compared to the true, input, force histories, and do not include the variability in time-function shape observed in association with differences in iceberg aspect ratio or mass, use of these models in the CSF inversion greatly improves estimates of seismic amplitude. Model C appears to be the best choice among the models tested, producing low misfit values and leading to robust recovery of input maximum-force values.

In this section, we consider which source-model features are most important in producing reliable inversion results, and evaluate requirements for further improvement, including for top-out iceberg-calving events. We discuss the path forward for obtaining improved source parameters for glacial earthquakes in a routine and systematic fashion, and test the use of Model C on real data. We also discuss implications for interpretation of existing results in the published glacial-earthquake catalog, which were derived using the 50-s-boxcar model.

5.1. Key Components of an Improved Seismic-Source Model

Our goal is a simple yet useful representation of the glacial-earthquake source, and we therefore consider which features control how well source parameters are recovered. Given the long (100s of seconds) force histories of the laboratory, field, and numerical constraints, it is surprising that the 50-s boxcar model recovers source parameters as well as it does, despite having a duration <10% that of the synthetic sources we test, and a symmetric shape. It is likely that the boxcar model works well because it contains a rapid force reversal that is similar to that contained in all of the input synthetic sources. This rapid change in force dominates the seismic-wave excitation, and its inclusion in the source model leads to better fits to the data. The rapid change in force also controls estimates of earthquake timing. In all cases we test, the earthquake time estimate from CSF inversion (the centroid time)

produces alignment of the simplified model time function with the rapid force reversal in the true source history, rather than, for example, alignment between the peak force values in the true and model force histories (Figure 8).

Models A, B, and C also contain rapid force reversals, and recover source parameters well; Model B, which has a peak-to-peak force-reversal amplitude that is half that of Model C over the same interval (Figure 8), fits the data worse than Models A and C. We test an additional 16 models to investigate the effect of model shape on input-value recovery, and find that models that lack a steep force reversal and instead reverse the force orientation over a longer time interval have higher misfits and poorer recovery of input parameters. For example, a sine-wave model with a period of 200 s returns synthetic seismograms that fit the input data poorly, producing misfit values around 0.9, and recovers maximum-force values poorly. All models we construct with a rapid force reversal recover input parameters more accurately than models with more gradual force reversals.

In addition to the rapid force reversal, the shapes of the left- and right-hand sides of the models play a role in the recovery of input parameters. We test simple models that approximate the general shape of Model C, but with the left-hand, tank-average shape replaced by a right triangle, and the right-hand side represented by an opposing right triangle of equal area. Despite capturing the rapid force reversal, these symmetric models do a poorer job recovering input parameters than Models A–C. Asymmetric models using a right triangle for the left-hand side do a similar job recovering input parameters to models constructed using tank-experiment constraints for the left-hand side (such as Models A–C), and might provide a good basis for future approaches allowing scaling of the time function by initial estimates of earthquake size or other parameters.

Models with low amplitudes of the right-hand side compared to the left-hand side (like Model B) do not recover maximum force or M_{CSF} values as well as Models A or C. Models with right-hand-side durations equal to or greater than the left-hand side, such as Model B (Figure 6), also result in poor fits to the data. We also find very poor fits to the seismograms using models that entirely omit the right-hand side, such as a model constructed using the tank-average left-hand-side but stopping at the first zero crossing of the force. This result suggests that the force history beyond the first zero crossing plays an important role in seismic-signal generation in the frequency band of interest. As expected, a more complicated model that mimics the complexity of the input force and includes multiple zero crossings, such as that illustrated in Figure 4d, recovers input force values well. However, because we do not yet have a full understanding of the source of the force oscillations that follow the primary force reversal, and because of the variability of this part of the signal between tank experiments, we limit further consideration to models containing a single force reversal and simple shapes. Model C, which captures the high-amplitude force reversal observed in the tank experiments and has a right-hand duration of 200 s, provides the best fit to data of the ∼20 models we test.

Our finding that the use of time functions like Models A and C leads to significantly better recovery of seismic magnitude values than the boxcar model, despite the fact that waveform fits are comparable between the two types of models, highlights a limitation of the long-period seismic data. These data are insufficiently sensitive to the shape of the source time function to discriminate one source time function from another based on waveform fits alone, as previously recognized by Tsai and Ekström (2007) and Tsai et al. (2008), as long as the source shapes in question include the key characteristics described here. However, our results demonstrate that including knowledge of the source shape derived from other datasets can markedly improve recovery of glacial-earthquake size.

5.2. Limitations on Direct Inversion for Force History

An open question remains whether more flexibility in the CSF inversion could be provided, within the limits of waveform sensitivity, by inverting for the source time function along with other parameters, with the time function parameterized by a small number of simple shapes. This approach has been used successfully to obtain more detailed source histories for landslides (e.g., Ekström & Stark, 2013). We experiment with using the Landslide-Force-History (LFH) technique (Ekström & Stark, 2013) to invert directly for the shape of the glacial-earthquake force function. In these inversions we restrict the force function to consist of a small number (4–8) of isosceles triangles overlapping by 50%. We solve for the amplitude of each triangular sub-source, and allow horizontal and vertical forces to vary independently. To minimize oscillation in the force functions we apply a weak smoothing constraint to these models. The force histories are constrained to integrate to zero.

We find that a simple 50-s LFH model with four sub-sources overlapping by 50% reproduces the input force to within 50% (Figure 7a). Misfits for these experiments are higher than those using a boxcar model, but are within

the range found for published glacial earthquakes. Extending the duration of the four sub-sources to 40 s, resulting in a full source duration of 100 s, produces maximum-force values similar to results using a 50-s LFH model, and similar fits to data. Though all evidence points to a source time function that is significantly longer than 100 s, experiments that further lengthen the duration of each sub-source lead to poor parameter recovery and high misfits. This is likely due to the fact that a rapid force reversal is not captured by an LFH source when long-duration sub-sources (≥50 s) are used. We also experiment with increasing the number of shorter-duration (10–20 s) sub-sources as an alternative way to increase the full source duration. However, larger numbers of sub-sources lead to force histories that contain multiple rapid force oscillations that are inconsistent with our knowledge of the left-hand side of the source, even with the damping constraint. In addition, these experiments frequently return down-glacier force orientations, 180° from the input orientation.

Applying the LFH approach to real glacial-earthquake data produces similarly unsatisfactory results. For 10 glacial earthquakes that occurred at Helheim Glacier and Jakobshavn Isbræ, we find high misfit values (0.4–0.8) using the model with 40 s sub-source duration, and force histories that oscillate in what we believe to be a non-physical way for many of the glacial earthquakes using the 70- and 80-s models, similar to the behavior we observe in the experiments using synthetic seismograms. As for the experiments with fixed source shapes, we conclude that the available seismic data are, in general, not sufficient to constrain the shape of the glacial-earthquake source time function on their own. While the LFH-modeling technique has proven successful with landslide data (Ekström & Stark, 2013), glacial-earthquake data constraints are poorer, owing in part to longer source-to-station distances for glacial earthquakes and poorer azimuthal station coverage.

Sergeant et al. (2016) also investigated the possibility of solving directly for the force history of a glacial earthquake, using a deconvolution technique to estimate the source time function from displacement seismograms. However, the force histories they recover also contain rapid oscillations in both the horizontal and vertical forces that are not observed in any of the independent constraints from laboratory or field observations, and Sergeant et al. (2016) note that the rapid force oscillations have no physical basis.

While ideally we could obtain a description of the full force history directly from the seismic data, neither the LFH approach nor the approach of Sergeant et al. (2016) produces satisfactory results. The natural depletion of the glacial-earthquake seismograms in short-period energy, combined with sparse station coverage, make routine, independent estimation of the source time function infeasible at this time. The use of a fixed, but physically informed, time function is thus our preferred path forward for improving glacial-earthquake source-parameter estimates.

5.3. Maximum Force as a Preferred Metric of Glacial-Earthquake Size

The M_{CSF} value has been used in most studies of glacial earthquakes to date, including by the current authors, to provide a summary measure of earthquake size. The quantity was originally defined by Kawakatsu (1989) in an application of CSF inversion to landslides. As shown in Figure 4, it represents the integral of the momentum of the landslide mass or accelerating iceberg, with the static M_{CSF} value taken once the acceleration is complete (Figure 4c). In this sense, M_{CSF} is analogous to the seismic scalar moment M_0, which is the preferred summary measure of size for tectonic earthquakes and represents the seismic moment after fault slip is complete. Although the M_{CSF} value is well defined when the force history integrates to zero (e.g., Figures 4a–4c), and momentum is conserved within the limited region of the iceberg and calving front, it is clear from the tank data, GPS data, and numerical models that the momentum budget is not closed within this limited system. The momentum transfer that must occur to other parts of the Earth system does not appear to generate significant seismic energy, and, at this time, our knowledge of that longer-timescale component of the momentum budget is too limited to include in the source model for the glacial earthquakes.

As long as the true duration and shape of the glacial-earthquake source time function are unknown, serious limitations exist in the use of the M_{CSF} metric and its interpretation, primarily because values of M_{CSF} estimated from seismic data are highly sensitive to the shape and duration of the specified force-time function. However, our experiments show that the value of the maximum force acting during a glacial earthquake can be recovered robustly, and is far less sensitive to assumptions about the force-time history than is the M_{CSF} value (Figure 7). The maximum-force values (Figure 7a) are better recovered than are M_{CSF} values (Figure 7c) for both the traditional boxcar model and for our preferred model, Model C, for example. Furthermore, maximum-force values are recovered

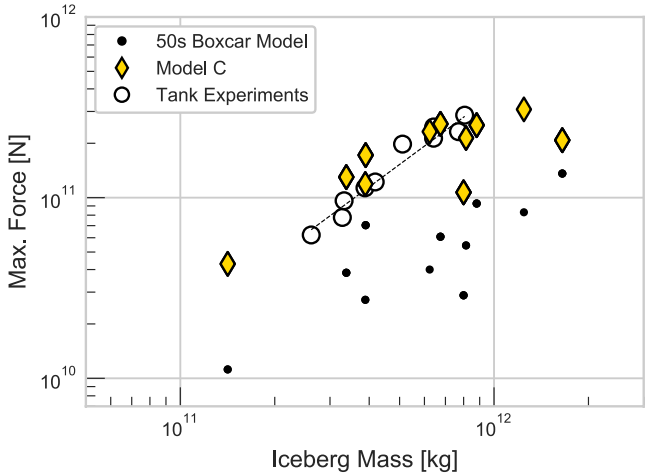

Figure 10. Maximum-force values versus iceberg mass for the glacial earthquakes shown as circles and squares in Figure 2 analyzed using (yellow diamonds) Model C and (black dots) a 50-s boxcar model. White circles show measured maximum-force values and iceberg masses from the ten scaled-up laboratory experiments used in this study. Dashed black line is fit to tank-experiment datapoints.

well across the full range of aspect ratios we test (Figure 7a; aspect ratio for each experiment given in Figure 5), whereas recovery of M_{CSF^*} values is notably poorer in experiments with higher iceberg aspect ratios (Experiments 7–10, Figure 7c). We therefore suggest that, at this time, the maximum force provides a better, simple measure of glacial-earthquake size than the M_{CSF} value that has been reported to date in the glacial-earthquake literature (Olsen & Nettles, 2017, 2019; Tsai & Ekström, 2007; Veitch & Nettles, 2012). We note that Sergeant et al. (2019) also considered the maximum force generated during a rotational calving event, and discussed advantages to this size metric as opposed to M_{CSF}.

5.4. Relationship Between Maximum Force and Iceberg Mass

For the tank experiments, the iceberg mass correlates with all three measures of glacial-earthquake size we consider: maximum force, maximum impulse, and M_{CSF^*}, where these values are read from the recorded force histories (gray squares in Figure 9). The dominant relationship in all cases is an increase in the seismic-magnitude parameters with increasing iceberg size. Analog icebergs with aspect ratios of 0.22 and 0.28 demonstrate a slightly different trend than those with aspect ratios of 0.43 and 0.54 (Figure 9a), owing to the higher peak amplitudes of the down-glacier force recorded in experiments of larger aspect ratio, compared with those of smaller aspect ratio (Figure 5).

Like the direct observations of force from the tank experiments, the seismic-magnitude values recovered using all five of the models discussed in detail in this study correlate positively with iceberg mass (Figure 9). Models A, B, and C do a better job capturing the relationship between iceberg mass and maximum force than does the boxcar model (Figure 9a). Despite the simplicity of Models A, B, and C, they each capture the difference in trend between larger and smaller aspect ratios that the tank observations display. In particular, maximum-force values recovered using Model C match the trend of the tank observations well for both small and large aspect ratios, and recover maximum-force values very close to the tank values (Figure 9a).

Improved recovery of all three seismic-magnitude metrics using Models A and C (Figures 7 and 9) is encouraging, and suggests the potential utility of reanalyzing real glacial-earthquake data using a more-sophisticated model. We use Model C in an analysis of 12 glacial earthquakes previously studied using the 50-s boxcar model (circles and squares in Figure 2) to test the approach. We find that maximum-force values are positively correlated with iceberg mass (yellow diamonds, Figure 10), as they are for the results with the boxcar model (black dots in Figure 10). As expected from our synthetic experiments, maximum-force values recovered using Model C are higher than those calculated for the same events using the boxcar model. The values for the real earthquakes obtained using Model C occupy approximately the same space in the maximum-force versus mass diagram as the values from the scaled-up tank experiments (Figure 10), suggesting that the values are likely to be realistic.

Sergeant et al. (2019) use a different approach to investigate the relationship between seismic magnitude and iceberg size. They estimate force histories using a deconvolution technique, and compare these histories to band-pass-filtered, numerically modeled force histories for capsize of a range of iceberg sizes. By performing a grid search over possible modeled force histories, they identify the height and iceberg aspect ratio of the model that most closely fits the data. They then consider a range of plausible iceberg cross-flow-length values and calculate an average volume estimate for a single iceberg. The iceberg volumes estimated using this technique come from model results, with limitations discussed earlier, and are not constructed by independent observations of iceberg size. Whereas we observe only a minor dependence of seismic-magnitude parameters on iceberg aspect ratio, a clear aspect-ratio dependence is observed in the relationship reported by Sergeant et al. (2019) between maximum force and model predictions of iceberg size. We discuss the need for further exploration of aspect-ratio dependence in Section 5.7.

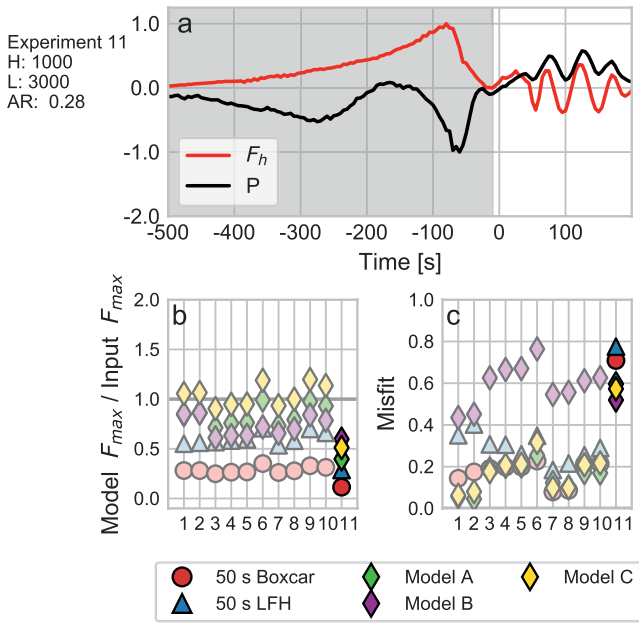

Figure 11. Analysis of a top-out iceberg-calving event. Panel (a) shows the horizontal force and pressure histories for the top-out event, presented in the same way as for the ten bottom-out calving experiments in Figure 5. Scaled-up dimensions for the analog iceberg height (H) and length (L) are given in m, along with iceberg aspect ratio (AR). Panels (b) and (c) show results of waveform modeling for this event using five different source models. Values from analysis of the bottom-out experiments are shown with lighter shading, as in Figure 7.

5.5. The Boxcar Model and Implications for Published Results

All evidence points to a true glacial-earthquake source duration longer than 50 s, which means that the M_{CSF} values reported in the glacial-earthquake literature almost certainly underestimate true M_{CSF} values, possibly by more than an order of magnitude. However, this underprediction appears to depend little on iceberg aspect ratio or mass, explaining the good observed correlation between iceberg size and M_{CSF} (Figure 2) and results using the more sophisticated source models evaluated here (Figures 9 and 10). Maximum-force values can be calculated from the M_{CSF} values estimated in previous studies using a boxcar-shaped model (Olsen & Nettles, 2017, 2019; Tsai & Ekström, 2007; Veitch & Nettles, 2012) in a straightforward manner. For a boxcar model like that shown in Figure 4a, $M_{CSF} = F_{max} \cdot (T_H)^2$, where T_H is the half duration of the force function, or 25 s for a 50-s boxcar model. Our results suggest that multiplication of these maximum-force values by a factor of 3–4 would bring them close to the likely true values (Figure 7a).

5.6. Top-Out Calving Events

As noted earlier, top-out calving events, in which the top surface of the iceberg rotates outward towards the fjord and the bottom of the berg rotates towards the calving face, are believed to be rare in comparison with bottom-out calving events. However, some such events are known to occur, and data are available from one analog experiment of top-out iceberg calving. We therefore explore source-parameter recovery for this, single, experiment using the same approach as for the bottom-out events. In laboratory experiments, top-out iceberg capsize occurs only when an initial angle of rotation for the iceberg is enforced, in contrast to the spontaneous capsize observed for bottom-out calving experiments (Amundson et al., 2012; Cathles et al., 2015). The experimental setup for top-out calving experiments is otherwise the same as for bottom-out experiments, and we follow the same data-processing and inversion steps.

The horizontal force and pressure histories recorded during the top-out experiment, which used an analog iceberg of aspect ratio 0.28, are shown in Figure 11a. The horizontal-force time series generated by top-out calving lacks the negative-force excursion observed in bottom-out experiments just after $t = 0$ s ("b" in Experiment 1, Figure 5), and the top-out pressure time series is more variable in the first 500 s than in bottom-out experiments. After $t = 0$ s the horizontal force and pressure histories from the top-out calving experiment smoothly transition to in-phase oscillation similar to that observed in bottom-out calving experiments.

As for the bottom-out experiments, waveform modeling recovers the force azimuth for the top-out experiment to within less than one degree. The maximum force observed in the top-out calving event is recovered better using Models A, B, and C than using the 50 s boxcar model, as is true for all of the bottom-out events (Figure 11b). However, the maximum force recovered is underestimated using all of the models, and using our preferred Model C, is only 0.5 of the input-force value. The misfit to the waveforms is high for all models, and for Model C is 0.6, much higher than the average misfit (0.17) for the 10 bottom-out calving experiments using Model C (Figure 11c).

As discussed in Section 2.2.1, the main glacial-earthquake signal is likely generated by the rapid force reversal around $t = 0$ s observed in the ten bottom-out calving experiments as well as in field observations from Helheim Glacier (Murray, Nettles, et al., 2015). The underestimation of the maximum-force value for the top-out experiment therefore likely comes from the fact that the source models used (boxcar, A, B, C) contain a deceleration phase that includes negative force values immediately following $t = 0$ s (Figure 6), while the tank-recorded force history (Figure 11a) does not. This interpretation is supported by the observation that Model B, which has the smallest negative-force excursion of the models considered here (Figure 6) both does the best job recovering

the maximum-force value for the top-out experiment and has the lowest misfit (Figure 11c), in contrast with the results for the bottom-out events.

Future work on these events could investigate whether high misfit values for top-out calving events might be a reliable diagnostic tool to separate top-out events and to flag them for further analysis. Such an approach might then be the first step in a workflow using a separate top-out source model, optimized to work with these less-common events.

5.7. Future Considerations in Source-Model Development

The work in this study demonstrates the feasibility of, and important improvement from, incorporating physics-based information into the glacial-earthquake source model, and provides a framework for future work. Further improvements to modeling of the glacial-earthquake source can build upon this proof-of-concept study by increasing the sophistication of the seismic-source parameterization used in the inversion procedure; and conducting additional analog calving experiments to elucidate the full nature of the seismic source.

In the current study, we maintained the requirement used in previous CSF analyses of glacial earthquakes that the shapes of the vertical and horizontal force histories be the same. Because laboratory and geodetic field data show that the shapes are indeed very similar prior to the force reversal, and because the vertical force amplitude is typically less than 20% that of the horizontal, this simplifying assumption was justified in our proof-of-concept study. However, future work should investigate possible improvements from using models with different shapes for the horizontal and vertical force histories. Constructing a model for the vertical force history using pressure records from laboratory experiments, converted to vertical force, might improve source-parameter recovery: our results suggest that the iceberg deceleration phase (i.e., the right-hand side of the source), may be more important to generation of the seismic signal than previously recognized, and it is during this time that the vertical- and horizontal-force histories differ most in shape.

Future work might also explore the utility of scaling the shape or duration of the force-time model based on iterative estimation of glacial-earthquake size. Such an approach is standard in CMT analysis of tectonic earthquakes (Ekström & Nettles, 2014), and may aid in modeling of glacial earthquakes, particularly in light of the range of iceberg sizes now known to generate glacial earthquakes (Olsen & Nettles, 2019).

Similarly, future tank experiments designed specifically to advance understanding of the glacial-earthquake source would be valuable. The role iceberg aspect ratio plays in determining the shape of the force history should be explored further, with additional laboratory experiments using analog icebergs with a larger range of aspect ratios. Uncertainty regarding the character of the right-hand side of the seismic source is currently a limitation, and obtaining data from the region of the tank away from the calving front might help clarify important aspects of the source. Because no geodetic field observations exist of top-out calving, analog experiments offer the primary means to explore this calving geometry. Additional tank experiments of top-out calving would aid exploration of the variability of force and pressure histories generated by iceberg capsize with this geometry (e.g., for icebergs with a range of aspect ratios), and could potentially be used to develop a source model specifically for top-out calving events. Numerical modeling that includes hydrodynamic forces, and the right-hand side of the force history, would also be helpful; some such work is currently underway (Bonnet et al., 2020).

6. Conclusions

In this study we have explored the feasibility of improving estimates of glacial-earthquake source parameters through incorporation of improved knowledge of the earthquake source time function. In particular, we have explored the utility of replacing the boxcar-shaped function used in previous work (Olsen & Nettles, 2017, 2019; Tsai & Ekström, 2007; Veitch & Nettles, 2012) with a more sophisticated time function based on knowledge obtained from laboratory, field, and numerical-modeling studies (Cathles et al., 2015; Murray, Nettles, et al., 2015; Sergeant et al., 2018).

We demonstrate that use of a source model that closely represents the true source of seismic waves (as is the case in this study for Model C and the synthetic seismograms we generate using tank-experiment observations), robustly retrieves source parameters of a seismic event. Even without a full physical description of the glacial-earthquake source, greatly improved estimates of source parameters can be obtained by this straightforward extension of the centroid-single-force modeling approach. We find that the rapid reversal in force, from upglacier

to downglacier, that occurs as a calving iceberg nears horizontal is the most important feature to include in the force-time model. This finding likely explains the success of the highly simplified, boxcar, model used in earlier studies. Previous numerical-modeling work (Sergeant et al., 2018) focused exclusively on the acceleration phase of the glacial-earthquake source; however, we find that the deceleration phase of the source time function also plays a role in generating waveforms that has not previously been appreciated.

The force-time model that we found to provide a good balance of simplicity and effectiveness in our proof-of-concept study, "Model C", captures the gradual force onset observed in the acceleration phase of the laboratory experiments we investigate. It contains the rapid force reversal from up to downglacier, and contains a ~200 s deceleration phase. Model C recovers source parameters well for icebergs with a range of aspect ratios, an important finding given our limited knowledge of the true aspect ratios of capsizing icebergs. The waveform-modeling approach we apply in this study is simple, computationally efficient, and returns robust estimates of source parameters despite the data-quality limitations inherent to work with glacial earthquakes. By incorporating non-seismic constraints on the shape of the force history, we overcome limitations associated with the sensitivity of long-period seismic data and produce better recovery of seismic-magnitude values.

Using synthetic seismograms, we demonstrate that the maximum force generated by a calving iceberg can be more accurately retrieved than the twice-integrated force value, M_{CSF}. We therefore prefer maximum force as a seismically derived measure of glacial-earthquake size: it provides a simple metric that is far less sensitive to modeling choices than integrated measures. We find that maximum-force values associated with M_{CSF} values reported for events in the published glacial-earthquake catalog likely underpredict true maximum-force values by a factor of 3–4 owing to the short duration and fixed shape of the 50-s boxcar model used, but that the underprediction is nearly constant across iceberg mass and aspect ratio, allowing for simple reconstruction of more accurate values.

The results we derive here from constructing and implementing a new generation of physics-based seismic-source models are an important step towards obtaining more accurate relationships between iceberg mass and seismic observables, and between physical quantities controlling iceberg calving dynamics. These improvements also form an important step towards the use of glacial-earthquake data as a geophysical tool for mass-loss estimation.

Conflict of Interest

The authors declare no conflicts of interest relevant to this study.

Data Availability Statement

We acknowledge the use of seismic data from the Greenland Ice Sheet Monitoring Network (Clinton et al., 2014) and the Global Seismographic Network (NSF EAR-1851048). All seismic data are publicly available from the IRIS DMC (NSF EAR-1851048; https://ds.iris.edu/ds/nodes/dmc/). Data that underpin the figures in this manuscript are available in a repository on the Harvard Dataverse (https://doi.org/10.7910/DVN/P3Q8RA). Some seismic analyses were completed using the Python library ObsPy (Beyreuther et al., 2010). Figures were made using the Matplotlib Python library (Hunter, 2007).

Acknowledgments
K. G. Olsen was supported by an NSF Graduate Research Fellowship (DGE-1644869). K. G. Olsen and M. Nettles also acknowledge support from NSF grants EAR-1639131 and EAR-1936254. T. Murray and T. D. James were supported by Natural Environment Research Council grant NERC NE/I007148/1. J.C. Burton was supported by NSF grant DMR-1506446. We appreciate constructive comments from two anonymous reviewers and Associate Editor Paul Winberry, as well as feedback from G. A. Abers, G. Ekström, J. Kingslake, and S. C. Webb on an earlier version of the manuscript.

References

Amundson, J. M., Burton, J. C., & Correa-Legisos, S. (2012). Impact of hydrodynamics on seismic signals generated by iceberg collisions. *Annals of Glaciology*, *53*(60), 106–112. https://doi.org/10.3189/2012aog60a012

Amundson, J. M., Fahnestock, M., Truffer, M., Brown, J., Lüthi, M. P., & Motyka, R. J. (2010). Ice mélange dynamics and implications for terminus stability, Jakobshavn Isbræ, Greenland. *Journal of Geophysical Research: Earth Surface*, *115*(F1). https://doi.org/10.1029/2009JF001405

Beyreuther, M., Barsch, R., Krischer, L., Megies, T., Behr, Y., & Wassermann, J. (2010). Obspy: A Python toolbox for seismology. *Seismological Research Letters*, *81*(3), 530–533. https://doi.org/10.1785/gssrl.81.3.530

Bonnet, P., Yastrebov, V. A., Queutey, P., Leroyer, A., Mangeney, A., Castelnau, O., et al. (2020). Modelling capsizing icebergs in the open ocean. *Geophysical Journal International*, *223*(2), 1265–1287. https://doi.org/10.1093/gji/ggaa353

Burton, J. C., Amundson, J. M., Abbot, D. S., Boghosian, A., Cathles, L. M., Correa-Legisos, S., et al. (2012). Laboratory investigations of iceberg capsize dynamics, energy dissipation and tsunamigenesis. *Journal of Geophysical Research: Earth Surface*, *117*(F1), F01007. https://doi.org/10.1029/2011JF002055

Cathles, L. M., Kaluzienski, L., & Burton, J. C. (2015). Laboratory investigations of seismicity caused by iceberg calving and capsize. In *AGU Fall Meeting Abstracts* (*2015*, p. C43B-0803).

Clinton, J. F., Nettles, M., Walter, F., Anderson, K., Dahl-Jensen, T., Giardini, D., et al. (2014). Seismic Network in Greenland Monitors Earth and Ice System. *Eos, Transactions American Geophysical Union*, *95*(2), 13–14. http://doi.org/10.1002/2014eo020001

Dziewonski, A. M., & Anderson, D. L. (1981). Preliminary reference Earth model. *Physics of the Earth and Planetary Interiors*, *25*(4), 297–356. https://doi.org/10.1016/0031-9201(81)90046-7

Dziewonski, A. M., Chou, T.-A., & Woodhouse, J. H. (1981). Determination of earthquake source parameters from waveform data for studies of global and regional seismicity. *Journal of Geophysical Research: Solid Earth*, *86*(B4), 2825–2852. https://doi.org/10.1029/jb086ib04p02825

Ekström, G. (2011). A global model of Love and Rayleigh surface wave dispersion and anisotropy, 25–250 s. *Geophysical Journal International*, *187*(3), 1668–1686. https://doi.org/10.1111/j.1365-246X.2011.05225.x

Ekström, G., & Nettles, M. (2014). Long-period moment-tensor inversion: The global CMT project. *Encyclopedia of Earthquake Engineering*, *1*, 1–13. https://doi.org/10.1007/978-3-642-36197-5_291-1

Ekström, G., Nettles, M., & Abers, G. A. (2003). Glacial earthquakes. *Science*, *302*(5645), 622–624. https://doi.org/10.1126/science.1088057

Ekström, G., Nettles, M., & Dziewoński, A. M. (2012). The global CMT project 2004–2010: Centroid-moment tensors for 13,017 earthquakes. *Physics of the Earth and Planetary Interiors*, *200–201*, 1–9. https://doi.org/10.1016/j.pepi.2012.04.002

Ekström, G., Nettles, M., & Tsai, V. C. (2006). Seasonality and increasing frequency of Greenland glacial earthquakes. *Science*, *311*(5768), 1756–1758. https://doi.org/10.1126/science.1122112

Ekström, G., & Stark, C. P. (2013). Simple scaling of catastrophic landslide dynamics. *Science*, *339*(6126), 1416–1419. https://doi.org/10.1126/science.1232887

Enderlin, E. M., Howat, I. M., Jeong, S., Noh, M.-J., Angelen, J. H., & van den Broeke, M. R. (2014). An improved mass budget for the Greenland ice sheet. *Geophysical Research Letters*, *41*(3), 866–872. https://doi.org/10.1002/2013GL059010

Heller, V., Chen, F., Brühl, M., Gabl, R., Chen, X., Wolters, G., & Fuchs, H. (2019). Large-scale experiments into the tsunamigenic potential of different iceberg calving mechanisms. *Scientific Reports*, *9*(1), 1–10. https://doi.org/10.1038/s41598-018-36634-3

Hunter, J. D. (2007). Matplotlib: A 2D Graphics Environment. *Computing in Science & Engineering*, *9*(03), 90–95. https://doi.org/10.1109/MCSE.2007.55

James, T. D., Murray, T., Selmes, N., Scharrer, K., & O'Leary, M. (2014). Buoyant flexure and basal crevassing in dynamic mass loss at Helheim Glacier. *Nature Geoscience*, *7*(8), 593–596. https://doi.org/10.1038/NGEO2204

Kawakatsu, H. (1989). Centroid single force inversion of seismic waves generated by landslides. *Journal of Geophysical Research: Solid Earth*, *94*(B9), 12363–12374. https://doi.org/10.1029/JB094iB09p12363

MacAyeal, D. R., Abbot, D. S., & Sergienko, O. V. (2011). Iceberg-capsize tsunamigenesis. *Annals of Glaciology*, *52*(58), 51–56. https://doi.org/10.3189/172756411797252103

Moon, T., Joughin, I., Smith, B. E., & Howat, I. M. (2012). 21st-century evolution of Greenland outlet glacier velocities. *Science*, *336*(6081), 576–578. https://doi.org/10.1126/science.1219985

Murray, T., Nettles, M., Selmes, N., Cathles, L. M., Burton, J. C., James, T. D., et al. (2015). Reverse glacier motion during iceberg calving and the cause of glacial earthquakes. *Science*, *349*(6245), 305–308. https://doi.org/10.1126/science.aab0460

Murray, T., Selmes, N., James, T. D., Edwards, S., Martin, I., O'Farrell, T., et al. (2015). Dynamics of glacier calving at the ungrounded margin of Helheim Glacier, southeast Greenland. *Journal of Geophysical Research: Earth Surface*, *120*(6), 964–982. https://doi.org/10.1002/2015JF003531

Nettles, M., & Ekström, G. (2010). Glacial earthquakes in Greenland and Antarctica. *Annual Review of Earth and Planetary Sciences*, *38*, 467–491. https://doi.org/10.1146/annurev-earth-040809-152414

Nettles, M., Larsen, T. B., Elósegui, P., Hamilton, G. S., Stearns, L. A., Ahlstrøm, A. P., et al. (2008). Step-wise changes in glacier flow speed coincide with calving and glacial earthquakes at Helheim Glacier, Greenland. *Geophysical Research Letters*, *35*(24), L24503. https://doi.org/10.1029/2008GL036127

Olsen, K. G., & Nettles, M. (2017). Patterns in glacial-earthquake activity around Greenland, 2011–13. *Journal of Glaciology*, *63*(242), 1077–1089. https://doi.org/10.1017/jog.2017.78

Olsen, K. G., & Nettles, M. (2019). Constraints on terminus dynamics at Greenland glaciers from small glacial earthquakes. *Journal of Geophysical Research: Earth Surface*, *124*, 1899–1918. https://doi.org/10.1029/2019JF005054

Sergeant, A., Mangeney, A., Stutzmann, E., Montagner, J., Walter, F., Moretti, L., & Castelnau, O. (2016). Complex force history of a calving-generated glacial earthquake derived from broadband seismic inversion. *Geophysical Research Letters*, *43*(3), 1055–1065. https://doi.org/10.1002/2015GL066785

Sergeant, A., Mangeney, A., Yastrebov, V. A., Walter, F., Montagner, J.-P., Castelnau, O., et al. (2019). Monitoring Greenland ice sheet buoyancy-driven calving discharge using glacial earthquakes. *Annals of Glaciology*, *60*, 1–95. https://doi.org/10.1017/aog.2019.7

Sergeant, A., Yastrebov, V. A., Mangeney, A., Castelnau, O., Montagner, J.-P., & Stutzmann, E. (2018). Numerical modeling of iceberg capsizing responsible for glacial earthquakes. *Journal of Geophysical Research: Earth Surface*, *123*(11), 3013–3033. https://doi.org/10.1029/2018JF004768

Tsai, V. C., & Ekström, G. (2007). Analysis of glacial earthquakes. *Journal of Geophysical Research: Earth Surface*, *112*(F3), F03S22. https://doi.org/10.1029/2006JF000596

Tsai, V. C., Rice, J. R., & Fahnestock, M. (2008). Possible mechanisms for glacial earthquakes. *Journal of Geophysical Research: Earth Surface*, *113*(F3), F03014. https://doi.org/10.1029/2007JF000944

Veitch, S. A., & Nettles, M. (2012). Spatial and temporal variations in Greenland glacial-earthquake activity, 1993–2010. *Journal of Geophysical Research: Earth Surface*, *117*(F4), F04007. https://doi.org/10.1029/2012JF002412

Walter, F., Amundson, J. M., O'Neel, S., Truffer, M., Fahnestock, M., & Fricker, H. A. (2012). Analysis of low-frequency seismic signals generated during a multiple-iceberg calving event at Jakobshavn Isbræ, Greenland. *Journal of Geophysical Research: Earth Surface*, *117*(F1), F01036. https://doi.org/10.1029/2011JF002132